

A Hybrid Field Model for Open-Circuit Field Prediction in Surface-Mounted PM Machines Considering Saturation

L. J. Wu¹, Zhaokai Li¹, Xiaoyan Huang¹, Yunlong Zhong¹, Youtong Fang¹,
and Z. Q. Zhu², *Fellow, IEEE*

¹College of Electrical Engineering, Zhejiang University, Hangzhou 310027, China

²Department of Electronic and Electrical Engineering, University of Sheffield, Sheffield S1 3JD, U.K.

This paper presents a nonlinear hybrid field model to predict the open-circuit magnetic field distribution in surface-mounted permanent-magnet machines. It combines the complex permeance model (CPM) with the magnetic equivalent circuit (MEC). The saturation effect is accounted for in the CPM by considering the magnetic potential distribution on the stator bore, which is calculated by the MEC and can be transformed to the virtual current on the slot. The proposed model significantly improves the calculation accuracy for saturated machines, which is verified by the finite-element analysis and the experimental results.

Index Terms—Analytical model, complex permeance, magnetic equivalent circuit (MEC), permanent-magnet (PM) machines, saturation effect.

I. INTRODUCTION

PERMANENT-MAGNET (PM) machines are increasingly used in industrial applications due to their high efficiency and torque density [1]. In the design of PM machines, the magnet loss, iron loss, unbalanced magnetic force, and back electromotive force (EMF) under open-circuit condition are all important, which are calculated from the open-circuit field distribution of the PM machines. There are several methods available for predicting the magnetic field of PM machines under open-circuit condition, such as the finite-element method (FEM), the magnetic equivalent circuit (MEC) method, and analytical model. FEM has high accuracy and capability of nonlinear analysis, but it is time consuming and loses generality for machine design [2]. On the other hand, the MEC and analytical models are much faster and therefore preferred at the initial design and optimization stages.

The MEC method can easily incorporate the nonlinearity of iron properties. Nonlinear adaptive lumped parameter magnetic circuit model was proposed to predict the electromagnetic performance of flux-switching PM machines [3], [4]. Mi *et al.* [5] developed an equivalent magnetic circuit to consider the assembly gap and saturation for magnetic flux calculation. However, the MEC method is incapable of describing the details of air-gap field distribution in the electrical machines. Besides, the MEC of surface-mounted permanent-magnet (SPM) machine is difficult to obtain due to the inequality of the magnetic potential on the PM surface.

Analytical models based on the conformal mapping method can accurately predict open-circuit flux density in the air gap of the slotted machines. Zhu and Howe [6] introduced relative permeance function for the slotting effect, while

Žarko *et al.* [7] proposed complex permeance function which is more accurate but complicated. Moreover, the complex permeance could be used for electromagnetic field calculation of electrical machine in the frequency domain for time-effective application [8]. O’Connell and Krein [9] utilized the Schwarz–Christoffel (SC) transformation from the slotted domain into the slotless domain and obtained the magnetic field according to Hague’s field solution. Boughrara *et al.* [10] took into account the effect of arbitrarily curved magnet surfaces and achieved high accuracy for predicting air-gap field and torque using conformal mapping. Ramakrishnan *et al.* [11] compared the analytical field solutions using SC transformation and complex permeance function to provide a comprehensive analysis about the influence of the deformation resulted from conformal mapping. Min *et al.* [12] applied particle swarm optimization to the complex permeance model (CPM) for optimizing SPM machines.

Another analytical models accounting for slotting effect are based on the subdomain model to predict open-circuit field [13], [14]. Subdomain models were developed to predict the magnetic field distribution of SPM machines considering tooth tips in [15] and [16]. Besides, the subdomain model is capable to analyze different types of electrical machines including PM vernier machine [17], PM linear synchronous machine [18], and dual-rotor machine [19]. However, while these analytical models assume infinitely permeable iron, the saturation effect is a general phenomenon in the electrical machines and can hardly be neglected. It has significant meanings for machine design and also influences the electromagnetic performance of the electrical machine. To effectively use the iron material, the working point of iron is usually in the nonlinear zone. Hence, large errors are often observed in the analytical prediction.

Fast and accurate model is required for predicting the open-circuit performance of PM machines, which takes the saturation effect into consideration. Although Hemeida and Sergeant [20] calculated the field distribution in the iron part by the MEC based on the air-gap field solution predicted by

Manuscript received November 16, 2017; revised February 11, 2018 and March 13, 2018; accepted March 13, 2018. Date of publication April 11, 2018; date of current version May 16, 2018. Corresponding author: X. Huang (e-mail: xiaoyanhuang@zju.edu.cn).

Color versions of one or more of the figures in this paper are available online at <http://ieeexplore.ieee.org>.

Digital Object Identifier 10.1109/TMAG.2018.2817178

0018-9464 © 2018 IEEE. Personal use is permitted, but republication/redistribution requires IEEE permission.

See http://www.ieee.org/publications_standards/publications/rights/index.html for more information.

CPM, the MEC was not utilized to improve the accuracy. Hafner *et al.* [8], [21] improved the CPM by introducing a parameter to consider the saturation effect, but required FEM simulation to obtain such parameter. Mahmoud *et al.* [22] introduced local saturation factors to represent the stator and rotor saturation in reluctance synchronous machines and adjust the flux density distribution iteratively. The complex permeance function was preferred to account for the slotting effect as it achieved higher accuracy than the relative permeance function [22]. The complex permeance method was improved in [23]–[25] by equivalently adjusting the air-gap length to account for the slotting and saturation effects. The complex permeance was calculated based on an equivalent geometry that increased air-gap length and slot opening according to the MMF drops in the teeth and slots. In [23] and [24], the MMF drops in the teeth and slots were calculated from the air-gap flux density distributions predicted by the CPM neglecting saturation. Therefore, such MMF drops and corresponding equivalent geometry adjustment are not accurate enough. To solve this problem, a nonlinear MEC of the complete machine was utilized in [25] to get MMF drops in the teeth and slots accounting for saturation. Hanic *et al.* [26] presented a combined analytical–numerical method based on the conformal mapping and MEC for calculating the back EMF and cogging torque waveforms of saturated SPM machines. In this method, the iron saturation was represented as the equivalent current sheet on the stator bore. The PM was represented as equivalent current and exactly transformed in the conformal mapping. Therefore, it is the exact conformal mapping method with better accuracy, compared with the improved CPMs in [23]–[25]. However, all models in [23]–[26] are time consuming, since the conformal mapping is required for every rotor position. Besides, Laoubi *et al.* [27] proposed a hybrid analytical model to analyze PM linear machines based on the coupling of mesh-based MECs and analytical models. This approach required meshing in the stator iron core and slots to form the MEC and made it similar to the finite element (FE) analysis [27]. Sprangers *et al.* [28] presented a semi-analytical method based on the harmonic modeling technique to account for the finite permeability of soft-magnetic teeth. Currently, only linear soft-magnetic materials with finite permeability can be considered [28]. In addition, the subdomain model can be improved to consider the permeability of iron regions [29], [30]. In the spoke-type PM synchronous machines, Liang *et al.* [29] regarded the magnetic bridge as fan-shaped saturation region with constant permeability and therefore obtained the analytical solution based on the subdomain technique. Roubache *et al.* [30] considered the finite permeability of stator and rotor region in the subdomain model and therefore improved the prediction accuracy.

In this paper, a hybrid field model (HFM) which has the synergies of both CPM and MEC is developed for predicting the open-circuit field distribution of the SPM machines. The main contribution of this paper is to take the saturation effect into consideration in the analytical model. For the most analytical analysis of SPM machines, the saturation of iron core is neglected and its permeability is assumed to be infinite.

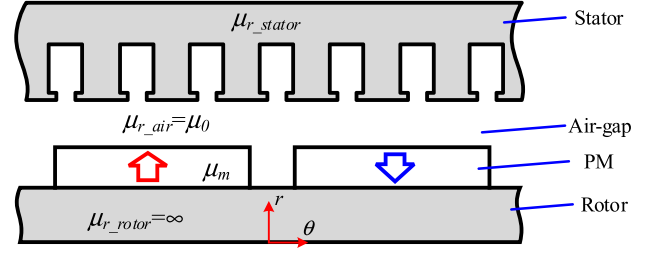


Fig. 1. Schematic view of SPM machine under open-circuit condition in polar coordinate.

This assumption may introduce errors for saturated machines. HFM can take the advantage of both CPM and MEC using the conception of equivalent current. It treats the magnetic potential distribution on the stator as the equivalent current to consider the saturation effect. The complex permeance function is calculated to describe the stator slotting and can be used at different rotor positions. Two 8-pole/48-slot SPM machines and a 10-pole/12-slot SPM machine are designed and analyzed by HFM, CPM, and FEM. The investigation shows that the proposed model has excellent accuracy in the prediction of the flux density and back EMF. Besides, HFM can save much computation time compared with FEM.

II. HYBRID FIELD MODEL

The nonlinear HFM to be described in this paper is derived with the following assumptions.

- 1) Linear magnet property with constant relative permeability.
- 2) All materials are isotropic.
- 3) No static/dynamic rotor eccentricities.
- 4) Infinitely permeable rotor iron, since the rotor iron is normally not saturated for better performance.
- 5) Negligible end effect. The influence of the permeance of stator iron is accurately considered in the model.

Fig. 1 shows the structure of the SPM machine in one pole-pair region. Stator slotting changes the magnetic field distribution in the air gap. Thus, the HFM is introduced to consider the stator saturation and slotting effect, as shown in Fig. 2. The slotted SPM machine is transformed into slotless machine using complex permeance function. The equivalent current is a replacement of magnetic potential drop in the stator iron to represent the saturation effect, and therefore iron permeability can be regarded as infinite. Then, the solution of Laplacian/quasi-Poissonian field equations in the air-gap region is obtained, which has taken into account the saturation effect.

A. Open-Circuit Field Solution Neglecting Slotting Effect

The open-circuit field in the air gap of the slotless PM machine is calculated by summing the field produced by PM neglecting the saturation effect and equivalent current, as shown in Fig. 2

$$B_{ocr} = B_{mr} + B_{sr} \quad (1)$$

$$B_{oca} = B_{ma} + B_{sa} \quad (2)$$

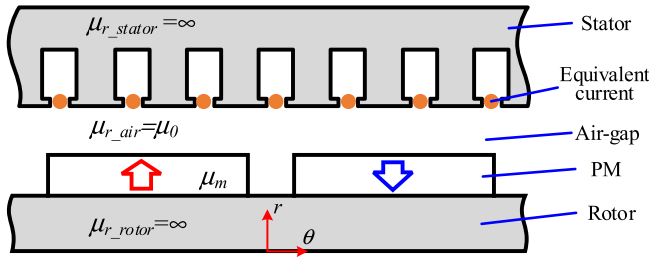


Fig. 2. HFM of SPM machine under open-circuit condition considering the saturation effect.

where B_{mr} and B_{ma} are the field components produced by the PM neglecting the saturation effect and B_{sr} and B_{sa} are the field components produced by the equivalent current of saturation.

The air-gap field distribution produced by PM neglecting saturation in a slotless machine can be expressed as [31]

$$B_{mr}(\theta, r) = \sum_{n=1,3,5,\dots}^{\infty} K_B(n) f_{Br}(r) \cos(np\theta) \quad (3)$$

for the radial component, and

$$B_{ma}(\theta, r) = \sum_{n=1,3,5,\dots}^{\infty} K_B(n) f_{B\theta}(r) \sin(np\theta) \quad (4)$$

for the circumferential component, where $K_B(n)$, $f_{Br}(r)$, and $f_{B\theta}(r)$ are given as follows.

When $np \neq 1$

$$K_B(n) = \frac{\mu_0 M_n}{\mu_m} \frac{np}{(np)^2 - 1} \frac{(A_{3n} - 1) + 2 \left(\frac{R_r}{R_m} \right)^{np+1} - (A_{3n} + 1) \left(\frac{R_r}{R_m} \right)^{2np}}{\frac{\mu_m+1}{\mu_m} \left[1 - \left(\frac{R_r}{R_s} \right)^{2np} \right] - \frac{\mu_m-1}{\mu_m} \left[\left(\frac{R_m}{R_s} \right)^{2np} - \left(\frac{R_r}{R_m} \right)^{2np} \right]} \quad (5)$$

$$A_{3n} = \left(np - \frac{1}{np}\right) \frac{M_{rn}}{M_n} + \frac{1}{np} \quad (6)$$

$$f_{Br}(r) = \left(\frac{r}{R_s}\right)^{np-1} \left(\frac{R_m}{R_s}\right)^{np+1} + \left(\frac{R_m}{r}\right)^{np+1} \quad (7)$$

$$f_{B\theta}(r) = -\left(\frac{r}{R_s}\right)^{np-1} \left(\frac{R_m}{R_s}\right)^{np+1} + \left(\frac{R_m}{r}\right)^{np+1} \quad (8)$$

when $np = 1$

$$K_B(n) = \frac{\mu_0 M_n}{2\mu_m} \frac{A_{3n} \left(\frac{R_m}{R_s}\right)^2 - A_{3n} \left(\frac{R_r}{R_s}\right)^2 + \left(\frac{R_r}{R_s}\right)^2 \ln \left(\frac{R_m}{R_s}\right)^2}{\frac{\mu_m+1}{\mu_m} \left[1 - \left(\frac{R_r}{R_s}\right)^2\right] - \frac{\mu_m-1}{\mu_m} \left[\left(\frac{R_m}{R_s}\right)^2 - \left(\frac{R_r}{R_m}\right)^2\right]} \quad (9)$$

$$A_{3n} = 2 \frac{M_{r1}}{M_1} - 1 \quad (10)$$

$$f_{Br}(r) = 1 + \left(\frac{R_s}{r}\right)^2 \quad (11)$$

$$f_{B\theta}(r) = -1 + \left(\frac{R_s}{r}\right)^2 \quad (12)$$

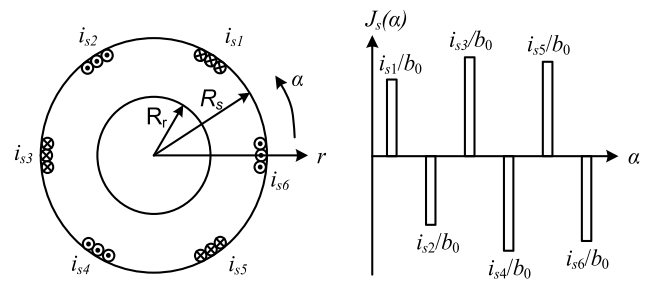


Fig. 3. Equivalent current sheet distribution on the stator bore.

where θ is the rotor angular position with reference to the axis of a magnet pole ($\theta = \omega_r t + \theta_0$, where θ_0 is the initial rotor position and ω_r is the mechanical angular velocity), r is the radial position, t represents the rotating time of the machine, μ_0 is the permeability of free space, μ_m is the relative recoil permeability of the PM, p is the number of pole pairs, R_s , R_m , and R_r are the radii of stator bore, magnet outer surface, and rotor yoke surface, respectively, and n is the order of the Fourier series terms, where M_n is defined as

$$M_n = M_{rn} + npM_{\theta n} \quad (13)$$

where for radial magnetization

$$M_{rn} = 2(B_r/\mu_0)\alpha_p \frac{\sin \frac{n\pi\alpha_p}{2}}{\frac{n\pi\alpha_p}{2}} \quad (14)$$

$$M_{\theta n} = 0 \quad (15)$$

and for parallel magnetization

$$M_{rn} = \frac{B_r}{\mu_0} \alpha_p (A_{1n} + A_{2n}) \quad (16)$$

$$M_{\theta n} = \frac{B_r}{\mu_0} \alpha_p (A_{1n} - A_{2n}) \quad (17)$$

where

$$A_{1n} = \frac{\sin \left[(np+1)\alpha_p \frac{\pi}{2p} \right]}{(np+1)\alpha_p \frac{\pi}{2p}}$$

$$A_{2n} = \begin{cases} 1, & np = 1 \\ \frac{\sin \left[(np-1)\alpha_p \frac{\pi}{2p} \right]}{(np-1)\alpha_p \frac{\pi}{2p}}, & np \neq 1 \end{cases} \quad (18)$$

where α is the stator angular position with reference to the axis of phase A winding, α_p is the magnet pole-arc to pole-pitch ratio, and B_r is the magnet remanence.

In order to calculate the magnetic field generated by the equivalent current, the expression from [6] representing the field produced by winding current should be rederived. As shown in Fig. 3, the current sheet is distributed uniformly on the slots of stator bore whose length is equal to the slot opening. The equivalent current, which is calculated from the MEC, has different values in different slots. From Fig. 3, the current density distribution on the stator bore can be

expressed as

$$J_s = \begin{cases} \frac{i_{sk}}{b_0}, & \frac{2k\pi}{Q_s} - \frac{b_0}{2R_s} \leq \alpha \leq \frac{2k\pi}{Q_s} + \frac{b_0}{2R_s} \\ 0, & \text{other } \alpha \end{cases} \quad k = 1, 2, \dots, Q_s \quad (19)$$

where b_0 is the slot opening, Q_s is the total number of slots, and i_{sk} is the equivalent current. As the sum of the stator current equals zero, the Fourier series expansion is obtained as

$$J_s = \sum_{k=1}^{Q_s} \sum_v \frac{2i_{sk}}{\pi b_0} \frac{1}{v} \sin\left(v \frac{b_0}{2R_s}\right) \cos\left(v\left(\alpha - \frac{2k\pi}{Q_s}\right)\right) \quad (20)$$

where v is the order of the Fourier series terms.

The governing Laplacian equation in polar coordinates is

$$\frac{\partial^2 \varphi}{\partial r^2} + \frac{1}{r} \frac{\partial \varphi}{\partial r} + \frac{1}{r^2} \frac{\partial^2 \varphi}{\partial \alpha^2} = 0. \quad (21)$$

As the permeability of the iron in the stator and rotor is infinite, the boundary condition for the air-gap field is [6]

$$\begin{cases} B_\alpha|_{r=R_r} = 0 \\ H_\alpha|_{r=R_s} = -J_s. \end{cases} \quad (22)$$

The general solution for the $\varphi(\alpha, r)$ is

$$\varphi(r, \alpha) = \sum_{k=1}^N \sum_v (A_v r^v + B_v r^{-v}) (C_{kv} \cos(v\alpha) + D_{kv} \sin(v\alpha)). \quad (23)$$

Hence, the radial and circumferential components of the magnetic field produced by the equivalent current are obtained as

$$B_{sr} = \frac{\mu_0}{\pi} \sum_{k=1}^{Q_s} \sum_v \frac{i_k}{v} K_{sov} F_v(r) \sin(v(\alpha - \alpha_k)) \quad (24)$$

$$B_{sa} = \frac{\mu_0}{\pi} \sum_{k=1}^{Q_s} \sum_v \frac{i_k}{v} K_{sov} G_v(r) \cos(v(\alpha - \alpha_k)) \quad (25)$$

where α_k is slot angular position, F_v , G_v , and K_{sov} are given by [6]

$$F_v(r) = \frac{v}{r} \left(\frac{r}{R_s}\right)^v * \frac{1 + \left(\frac{R_r}{r}\right)^{2v}}{1 - \left(\frac{R_r}{R_s}\right)^{2v}} \quad (26)$$

$$G_v(r) = \frac{v}{r} \left(\frac{r}{R_s}\right)^v * \frac{1 - \left(\frac{R_r}{r}\right)^{2v}}{1 - \left(\frac{R_r}{R_s}\right)^{2v}} \quad (27)$$

$$K_{sov} = \frac{\sin\left(v \frac{b_0}{2R_s}\right)}{v \frac{b_0}{2R_s}} \quad (28)$$

B. Effect of Slotting

In the 2-D field analytical model, the slotting effect is mainly analyzed by conformal mapping technique or subdomain technique. The key idea of subdomain technique is to directly solve the field governing equations in all subdomains, i.e., magnet, air gap, and stator slots, by applying the boundary conditions to the interfaces between these subdomains. As the subdomain technique precisely describes the slotting effect, the excellent accuracy for predicting magnetic field distribution can be achieved. However, since the subdomain technique requires to solving an inverse of a large matrix for each rotor position, it is time consuming [13]. On the other hand, for conformal mapping technique, e.g., CPM, the slotting effect is represented as a relative permeance, whose calculation is required only once for a specific geometry [7]. It is much simpler and faster, and therefore this paper aims at improving the original CPM to include the saturation effect. The fundamental idea of complex permeance function is to transform the actual slotted air gap into a slotless air gap using four conformal transformations [7], [32]

$$Z = \ln r_a + j * \theta_a \quad (29)$$

$$Z = j \frac{g'}{\pi} \left[\ln \left(\frac{1+p}{1-p} \frac{b-p}{b+p} \right) - 2 \frac{b-1}{\sqrt{b}} \tan^{-1} \frac{p}{\sqrt{b}} \right] + \ln R_s + j\theta_2 \quad (30)$$

$$p = \sqrt{\frac{w-b}{w-a}} \quad (31)$$

$$K = R_s e^{j \left(\frac{g'}{\pi} \ln w + \frac{\theta_s}{2} \right)} \quad (32)$$

$$\lambda = \frac{K}{r_a e^{\theta_a}} \frac{\omega - 1}{\sqrt{(\omega - a)(\omega - b)}} = \lambda_a + j\lambda_b \quad (33)$$

where λ is the complex relative air-gap permeance, r_a and θ_a are the air-gap positions of the machine in polar coordinates, $\theta_s = 2\pi/Q_s$, and a and b are described as

$$b = \left[\frac{b_0}{2g'} + \sqrt{\left(\frac{b_0}{2g'}\right)^2 + 1} \right]^2 \quad (34)$$

$$a = \frac{1}{b} \quad (35)$$

$$g' = \ln \frac{R_s}{R_r} \quad (36)$$

where θ_2 is the angle of the slot corner. As the relationship between the S -plane representing the original slot geometry and the K -plane representing slotless air gap is shown in (29)–(33), the radial and circumferential flux densities in the air gap of the slotted machine are described in the form of Fourier series

$$\begin{aligned} B_{\text{slot}_r} &= (B_{mr} + B_{sr})\lambda_a + (B_{ma} + B_{sa})\lambda_b \\ &= \left(\sum_{n=1}^{\infty} B_{\text{slot}_rn} \cos(nm(\alpha - \alpha_{rn})) \right) \lambda_a \\ &\quad + \left(\sum_{n=1}^{\infty} B_{\text{slot}_an} \cos(nm(\alpha - \alpha_{an})) \right) \lambda_b \end{aligned} \quad (37)$$

$$\begin{aligned}
B_{\text{slot}_a} &= (B_{ma} + B_{sa})\lambda_a - (B_{mr} + B_{sr})\lambda_b \\
&= \left(\sum_{n=1}^{\infty} B_{\text{slot}_{an}} \cos(nm(\alpha - \alpha_{an})) \right) \lambda_a \\
&\quad - \left(\sum_{n=1}^{\infty} B_{\text{slot}_{rn}} \cos(nm(\alpha - \alpha_{rn})) \right) \lambda_b \quad (38)
\end{aligned}$$

where m represents the rotational symmetry order.

C. Saturation Effect

The magnetic potential distribution of the stator, which represents the stator saturation, is calculated using the MEC method (see Fig. 4). The key idea of MEC is to replace the real iron with the magnetic tube. Following this principle, any stator with arbitrary geometry in SPM machines can be equivalently transformed into corresponding MEC [33], [34]. Therefore, the equivalent reluctance of the flux tubes is calculated and connected to form the magnetic network. The magnetic flux flowing in the stator is calculated from the air-gap field distribution and expressed as

$$\begin{aligned}
\phi_{s(2k-1)} &= R_s^- l_{\text{ef}} \int_{\alpha_k - b_0/2R_s}^{\alpha_k + b_0/2R_s} B_{\text{slot}_r}(\alpha, R_s^-, t) d\alpha \\
\phi_{s(2k)} &= R_s^- l_{\text{ef}} \int_{\alpha_k + \tau_t - b_0/2R_s}^{\alpha_k + \tau_t + b_0/2R_s} B_{\text{slot}_r}(\alpha, R_s^-, t) d\alpha \\
k &= 1, 2, \dots, Q_s \quad (39)
\end{aligned}$$

where l_{ef} is the effective axial length of a stator coil and $\tau_t = 2\pi/Q_s$. Thus, the magnetic potential distribution in the stator (e.g., $V_1, V_2, \dots, V_{6Q_s}$ in Fig. 4) is solved according to Kirchhoff's law

$$f(\mathbf{V}) = \mathbf{A}\mathbf{\Lambda}\mathbf{A}^T\mathbf{V} - \mathbf{\Phi} = 0 \quad (40)$$

where \mathbf{A} is the incidence matrix, $\mathbf{\Lambda}$ is the branch permeance matrix, \mathbf{V} is the node magnetic potential matrix, and $\mathbf{\Phi}$ is the node flux matrix which consists of ϕ_{sk} . The numerical solution of (40) is calculated based on the Newton-Raphson method.

When the converged solution is obtained, the magnetic potential distribution on the stator bore can be equivalently transformed to the equivalent current on the slot openings. The relationship between the magnetic potential distribution and equivalent current is expressed as

$$i_{sk} = -(V_{k+2} - V_k) \quad (41)$$

where V_{k+2} and V_k are the magnetic potentials in the adjacent stator teeth, e.g., V_{4Q_s+1} in Fig. 4, and they represent the saturation effect in the stator yoke and stator teeth. Equation (41) is the mathematical expression of the equivalent transformation from Figs. 1 to 2. The transformation from the magnetic potential distribution in the stator iron to the equivalent current in the slot makes the iron permeability become infinite, so that the analytical solution of the air-gap field can be easily calculated. In other word, the equivalent current of saturation i_{sk} is a replacement of magnetic potential drop in the stator iron to represent the saturation effect. Its value shows the saturation level of the corresponding stator iron. The negative sign in (41) means that the equivalent

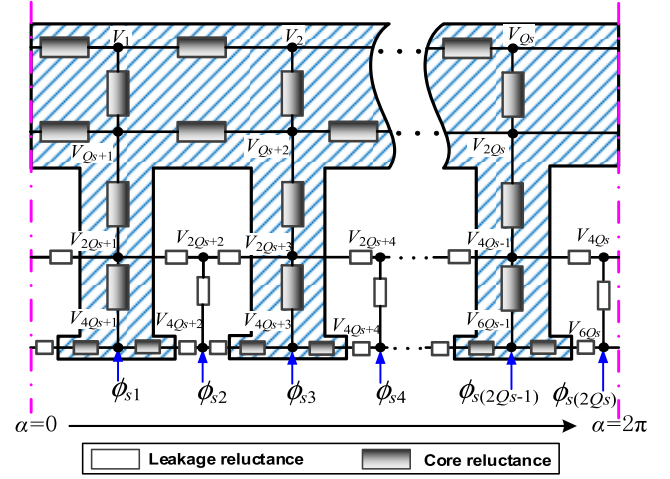


Fig. 4. MEC of the stator in the SPM machine.

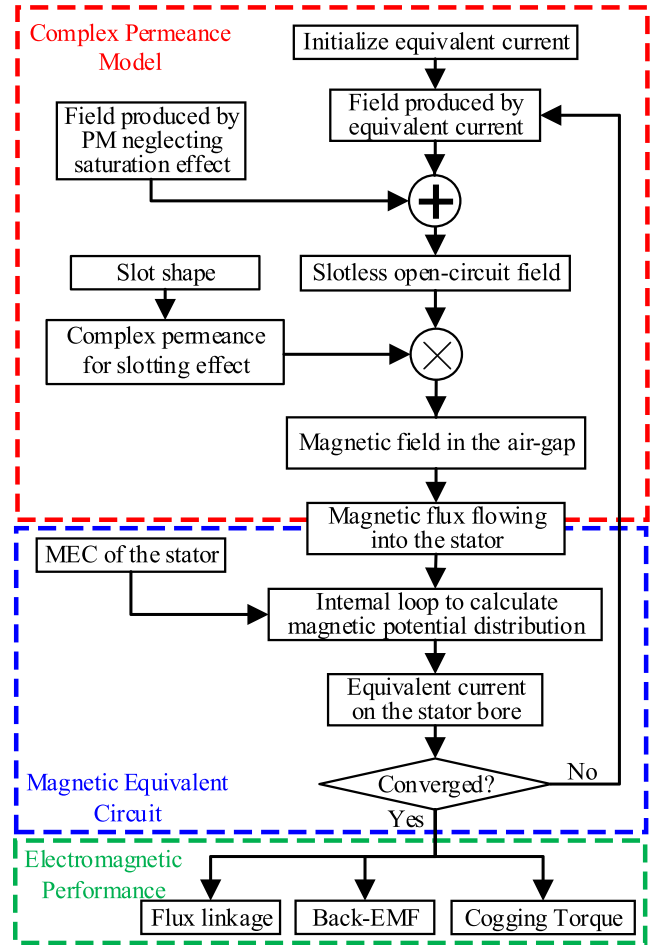


Fig. 5. General flowchart to calculate the magnetic field distribution using the HFM.

current will produce reverse field to decrease the amplitude of the original field.

Fig. 5 shows the calculation process for the saturated air-gap field distribution. The magnetic potential distribution can be obtained in the internal loop when the magnetic field distribution in the air gap is given. The analytical solution of

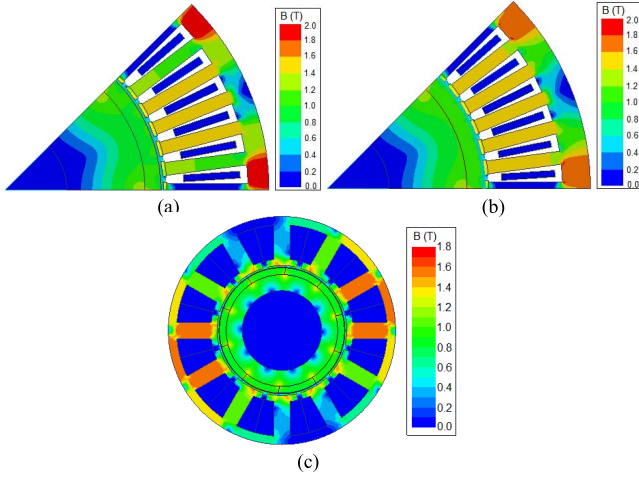


Fig. 6. Flux density distribution of prototype SPM machines with nonlinearly permeable iron. (a) Machine A: $h_{sy} = 6$ mm. (b) Machine B: $h_{sy} = 8$ mm. (c) Machine C: $h_{sy} = 3.7$ mm.

the slotted air-gap field can be obtained when the equivalent current is determined. Thus, the external loop in Fig. 5 is required to iteratively calculate the magnetic potential distribution and air-gap field distribution to reach convergence.

The proposed model is general. The MEC shown in Fig. 4 is applicable for any number of slots. In addition, the number of poles has no influence on the establishment of MEC. Such general model can be easily programmed although it is slightly complicated than the pure analytical model. Once it is programmed, it is very powerful for the machine design and analysis, especially for optimization.

D. Computational Complexity

Practically, the speed of solving a model depends on not only its computational complexity, but also the algorithm. In this section, the computational complexity of CPM, HFM, and FEM is analyzed and compared. The CPM is the simplest and fastest because it neglects the nonlinear property of iron core, and therefore no iteration is required at any rotor position. The calculation of the complex permeance function is needed only once in the initial preparation. The calculation of FEM for one rotor position requires solving a nonlinear $N_{\text{mesh}} \times N_{\text{mesh}}$ matrix, where N_{mesh} is the number of nodes in the FEM. It means that the computation time of FEM mainly depends on the mesh size. As for HFM, solving the stator MEC deals with a nonlinear $N_{\text{nd}} \times N_{\text{nd}}$ matrix, where N_{nd} is the number of nodes in the MEC. Analytical computation time in HFM is negligible because it only requires computing the linear equations (1)–(38). As N_{nd} is always much larger than N_{nd} , the computational complexity of FEM is much heavier than that of HFM.

III. ELECTROMAGNETIC PERFORMANCE

A. Flux Linkage and Back EMF

When the magnetic field distribution in the air gap of the PM machine under open-circuit condition is predicted, the flux

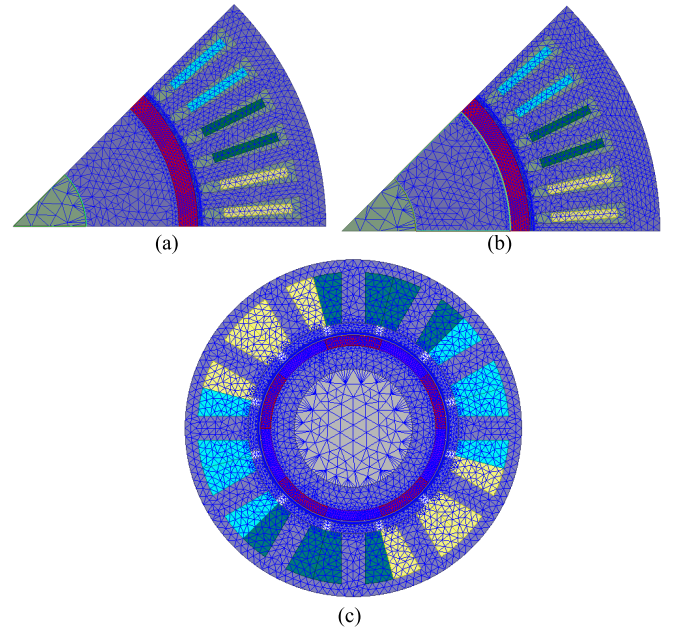


Fig. 7. Mesh distribution of prototype SPM machines. (a) Machine A. (b) Machine B. (c) Machine C.

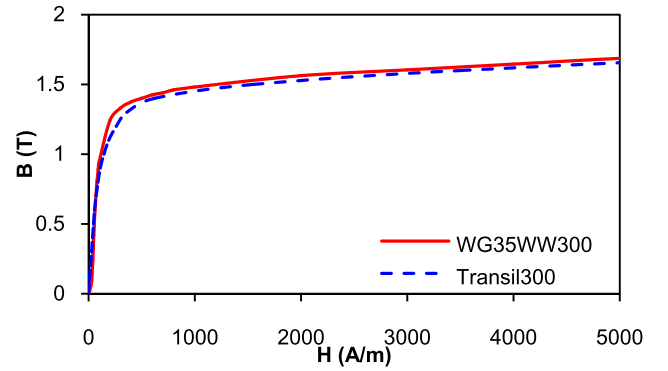


Fig. 8. B - H curves of the iron for prototype SPM machines.

linking a stator winding coil is calculated from

$$\varphi_i(t) = R_s^- l_{ef} \int_{\alpha_i - \tau/2}^{\alpha_i + \tau/2} B_{\text{slot}_r}(\alpha, R_s^-, t) d\alpha \quad (42)$$

where α_i and τ represent the angle of axis and coil pitch for one coil of any phase. The total flux linkage for any phase can be determined by summing the flux of individual coils which belong to the same phase [35]. However, this method neglects the flux leakage in the slot, which should be a part of the total flux linkage. In the proposed model, the slot flux leakage and tooth tip flux leakage are obtained from the MEC and the total flux linkage ψ_{ph} for one phase is expressed as

$$\psi_{ph}(t) = W * \sum_{i=1}^{\kappa} \left(\varphi_i(t) + \sum_{j=1}^{\gamma} \varphi_{ij}(t) + \sum_{j=1}^{\gamma} \varphi_{(i+\tau)j}(t) \right) \quad (43)$$

where W is the number of turns per slot for one phase, κ is the number of the coils of the same phase in different slots, γ

TABLE I
MAIN PARAMETERS OF PROTOTYPE SPM MACHINES

Parameter	Machine A/B	Machine C	Unit
Stator outer radius	75	50	mm
Stator inner radius	45	28.5	mm
Air-gap length	0.75	1	mm
Magnet thickness	4.5	3	mm
Rotor outer radius	44.25	27.5	mm
Shaft radius	17.5	17.5	mm
Active length	75	50	mm
Slot opening	1.5	2	mm
Tooth tip edge	1	2.8	mm
Tooth body width	3.72	7.1	mm
Pole-arc to pole-pitch ratio	1	1	
Magnet remanence	1.26	1.20	T
Relative recoil permeability	1.07	1.05	
Magnetization	Parallel	Parallel	
Rated speed	1500	400	rpm
Number of pole pairs	4	10	
Number of slots	48	12	
Lamination material	WG35WW300	Transil300	

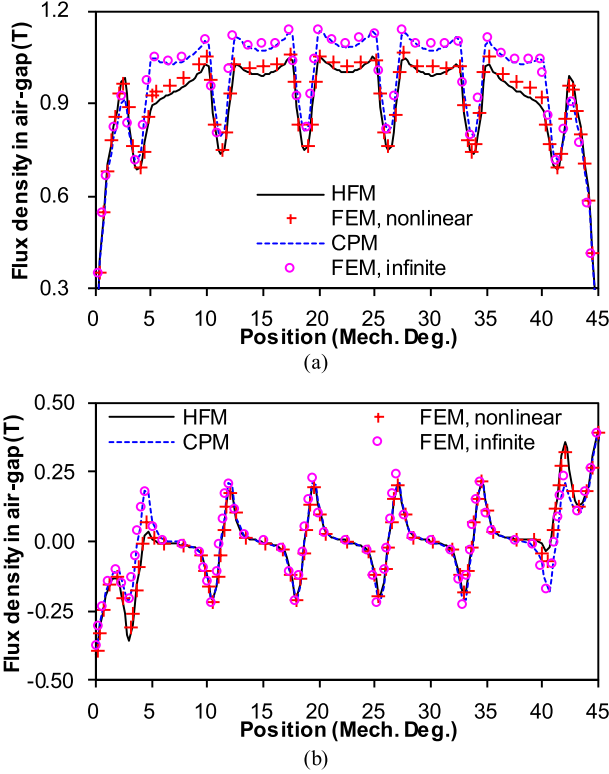


Fig. 9. HFM, CPM, and FEM predicted air-gap flux density waveforms in the middle of the air gap of Machine A under open-circuit condition. (a) Radial. (b) Circumferential.

is the layer of the tangential magnetic reluctance in one slot, and ϕ_{ij} and $\phi_{(i+)_j}$ are the tangential fluxes in the slot that covers coil. When the SPM rotor rotates, ψ_{ph} changes as well as the equivalent current and magnetic potential distribution. Thus, the back EMF can be obtained as

$$E_{ph} = -\frac{d\psi_{ph}}{dt} \quad ph = A, B, \text{ and } C. \quad (44)$$

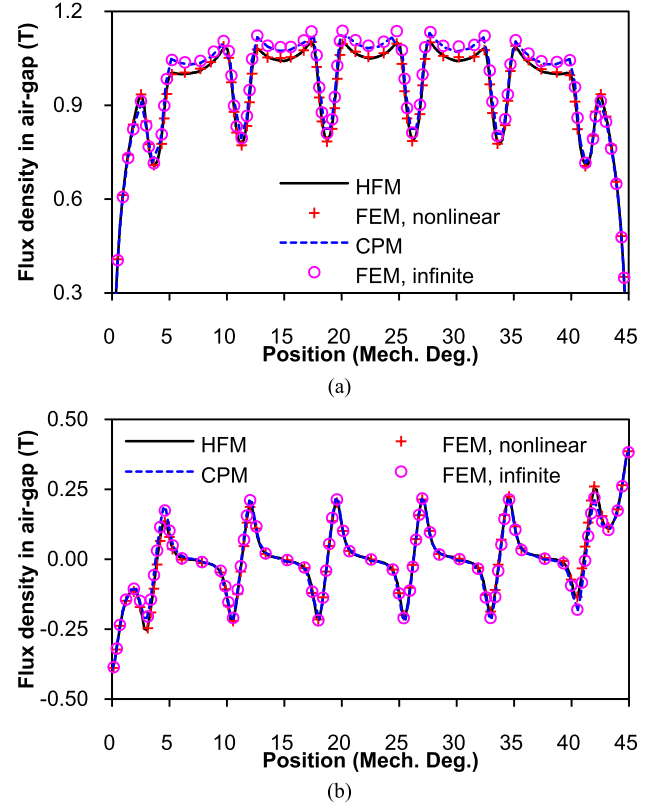


Fig. 10. HFM, CPM, and FEM predicted air-gap flux density waveforms in the middle of the air gap of Machine B under open-circuit condition. (a) Radial. (b) Circumferential.

B. Cogging Torque

The cogging torque can be calculated by integrating Maxwell's stress tensor along a circle with constant radius located inside the air gap once the radial and tangential components of flux density in the air gap are known [32]

$$\begin{aligned}
 T_c &= \frac{1}{\mu_0} l_{ef} r^2 \int_0^{2\pi} B_{slot_r}(\alpha, r, t) B_{slot_a}(\alpha, r, t) d\alpha \\
 &= \frac{1}{\mu_0} l_{ef} r^2 \int_0^{2\pi} \left(\sum_{n=1}^{\infty} B_{slot_{rn}} \cos(nm(\alpha - \alpha_{rn})) \right) \\
 &\quad * \left(\sum_{n=1}^{\infty} B_{slot_{an}} \cos(nm(\alpha - \alpha_{an})) \right) d\alpha \\
 &= \frac{1}{2\mu_0} l_{ef} r^2 \left(\sum_{n=1}^{\infty} B_{slot_{rn}} B_{slot_{an}} \cos(nm(\alpha_{an} - \alpha_{rn})) \right) \quad (45)
 \end{aligned}$$

IV. FE AND EXPERIMENTAL VALIDATION

In order to validate the proposed model, two 8-pole/48-slot SPM machines and a 10-pole/12-slot SPM machine are analyzed by HFM, CPM, and FEM (see Figs. 6 and 7). Their major parameters are given in Table I. The nonlinear $B-H$ curves of lamination materials are shown in Fig. 8. Machine A and Machine B have similar parameters, except the stator yoke height (h_{sy}). Machine A has smaller stator yoke height than Machine B, so they have different levels of saturation. Besides, Machine C has fractional semi-closed slots while Machine A/B

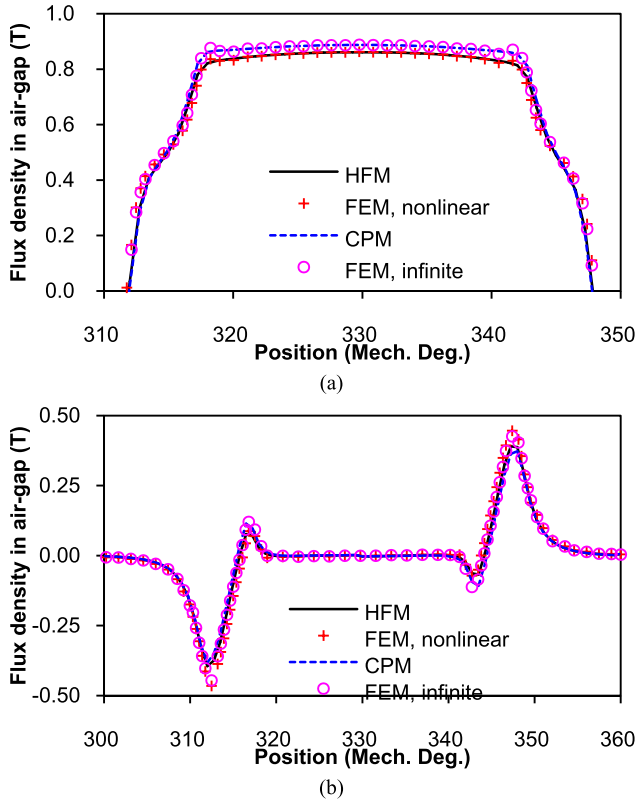


Fig. 11. HFM, CPM, and FEM predicted air-gap flux density waveforms in the middle of the air gap of Machine C under open-circuit condition. (a) Radial. (b) Circumferential.

has integer slots with small tooth tips, making the comparison more comprehensive and representative. In order to show the saturation effect by FE model, the FE analysis is performed for both infinitely and nonlinearly permeable iron.

Figs. 9–11 show the comparison between the HFM, CPM, and FEM predictions of flux density in the air gap for Machines A–C. The radial flux densities predicted by HFM agree well with nonlinear FEM results while CPM predicts higher radial flux density than nonlinear FEM for three machines. Besides, the differences of radial flux density between nonlinear FEM and infinite FEM show that the iron saturation has significant influence on the radial flux density in the air gap. As for the circumferential flux density, both HFM and CPM show high accuracy. However, the CPM predicts higher peak value close to the first and sixth slots compared with FEM and HFM for Machines A and B. Moreover, the CPM shows much larger errors for Machine A, which has smaller stator yoke height and heavier saturation effect. Therefore, the advantage of HFM is more significant in the analysis of machines with high saturation level. For Machine C, the circumferential flux densities predicted by CPM have larger errors than those predicted by HFM, when they are close to the slot. Besides, comparison between nonlinear and infinite FEM results of circumferential flux density for three machines shows that the saturation mainly influences the peak value of circumferential flux density, which is located close to the slot.

Figs. 12–14 show the comparison of the flux linkages predicted by HFM, CPM, and FEM for three machines. The saturation influences the peak value of the flux linkage, which

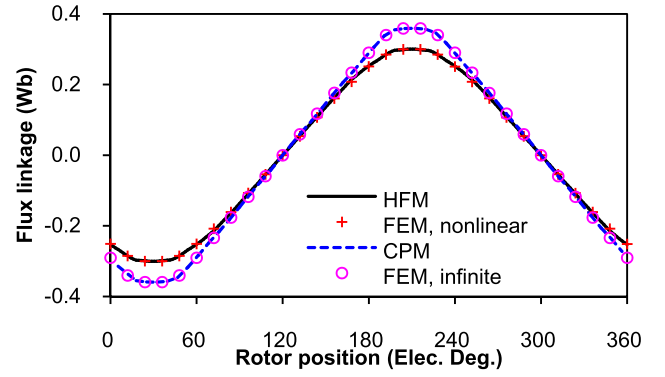


Fig. 12. HFM, CPM, and FEM predicted flux linkages of Machine A under open-circuit condition.

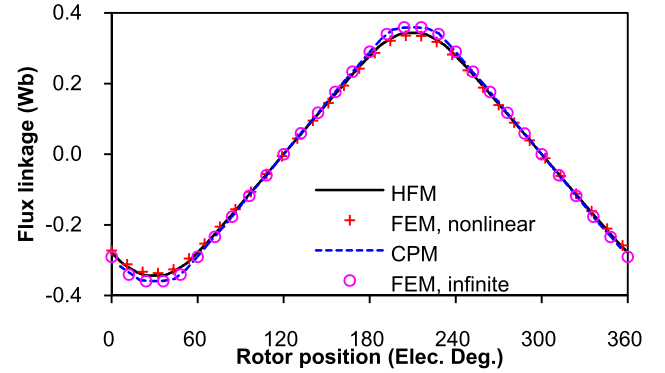


Fig. 13. HFM, CPM, and FEM predicted flux linkages of Machine B under open-circuit condition.

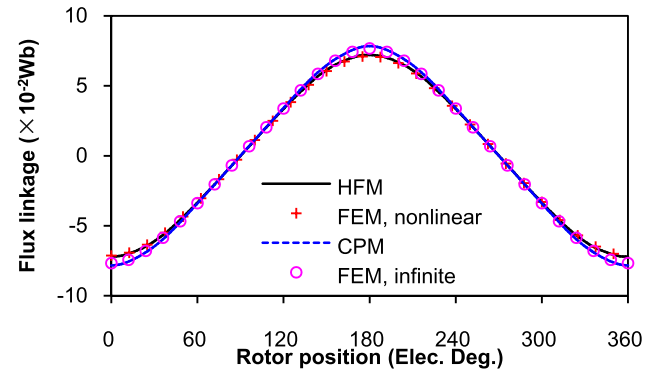


Fig. 14. HFM, CPM, and FEM predicted flux linkages of Machine C under open-circuit condition.

can be observed by comparison of nonlinear and infinite FEM predictions. HFM can accurately predict the waveform of flux linkage but CPM always overestimates its peak value for three machines.

As shown in Figs. 15–17, the infinite FEM predictions of back EMF has higher amplitude than the infinite FEM predictions, which results from the saturation effect. Figs. 15 and 16 illustrate that HFM can accurately predict back EMF while CPM overestimates the ripples and amplitudes of the back EMF for Machine A and Machine B. Meanwhile, the error of CPM prediction is larger in Machine A than Machine B

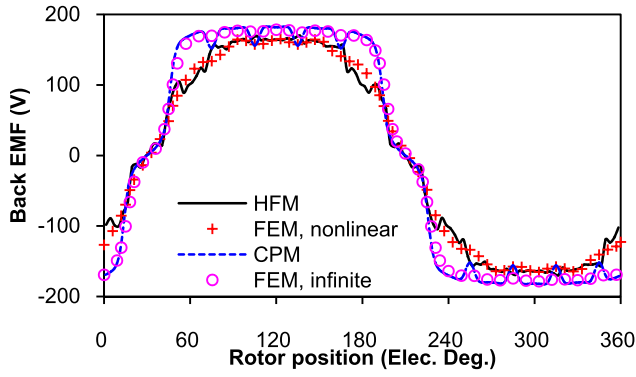


Fig. 15. HFM, CPM, and FEM predicted phase back EMF waveforms of Machine A under open-circuit condition.

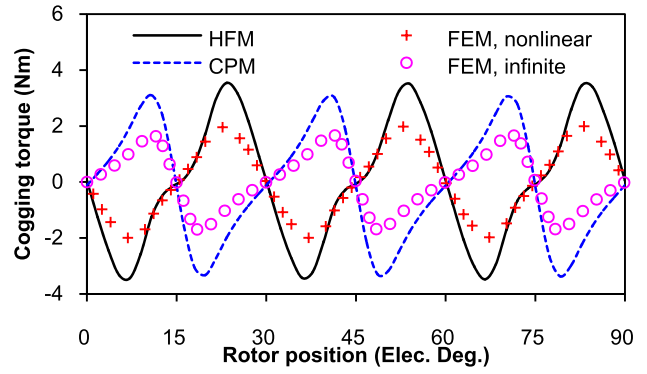


Fig. 18. HFM, CPM, and FEM predicted cogging torque waveforms of Machine A.

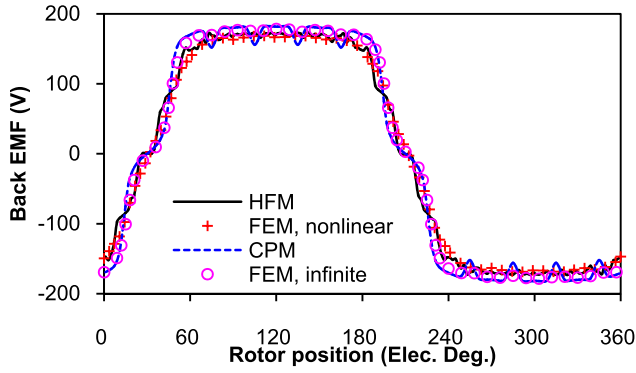


Fig. 16. HFM, CPM, and FEM predicted phase back EMF waveforms of Machine B under open-circuit condition.

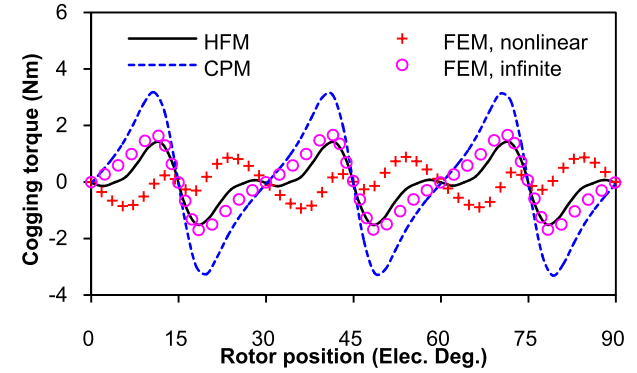


Fig. 19. HFM, CPM, and FEM predicted cogging torque waveforms of Machine B.

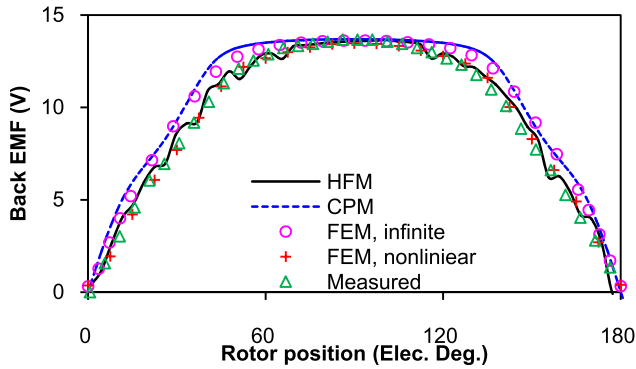


Fig. 17. HFM, CPM, and FEM predicted phase back EMF waveforms of Machine C under open-circuit condition.

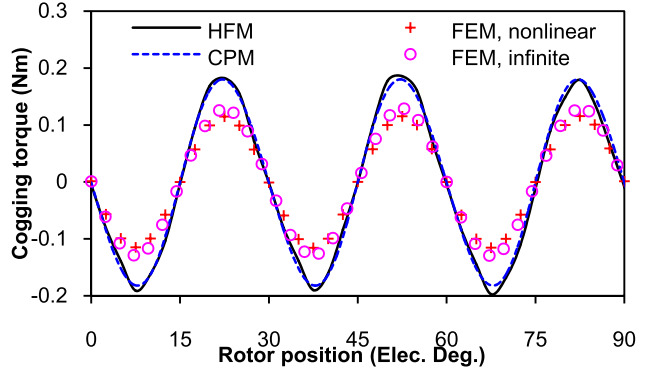


Fig. 20. HFM, CPM, and FEM predicted cogging torque waveforms of Machine C.

due to higher saturation in Machine A, but HFM consistently has excellent accuracy regardless of saturation level since CPM cannot take the saturation effect and flux leakage into consideration while HFM can overcome the disadvantage with the help of MEC. Fig. 17 shows the comparison of the back EMF waveforms predicted by HFM and CPM with the FEM and measured results for Machine C. HFM prediction agrees well with the measured and FEM results while CPM obtains higher back EMF values due to neglecting the saturation effect. Thus, the excellent accuracy of HFM for predicting back EMF of SPM machines is verified by both FEM and experimental results.

The cogging torque waveforms predicted by HFM, CPM, and FEM for three machines are compared in Figs. 18–20. It can be seen that the saturation effect greatly affects the shapes of cogging torque waveform for Machines A and B but slightly influence the amplitude of cogging torque for Machine C. From the comparison between nonlinear and infinite FEM predictions in Figs. 18 and 19, the stator saturation can even make the waveforms of cogging torque opposite. Since the saturation level in Machine A is more severe, its distortion of cogging torque due to saturation is more significant. The CPM prediction is the same for both Machines A and B due to neglecting the saturation effect, while the HFM prediction is influenced by the saturation level. Although the HFM considers the saturation, its prediction still shows larger

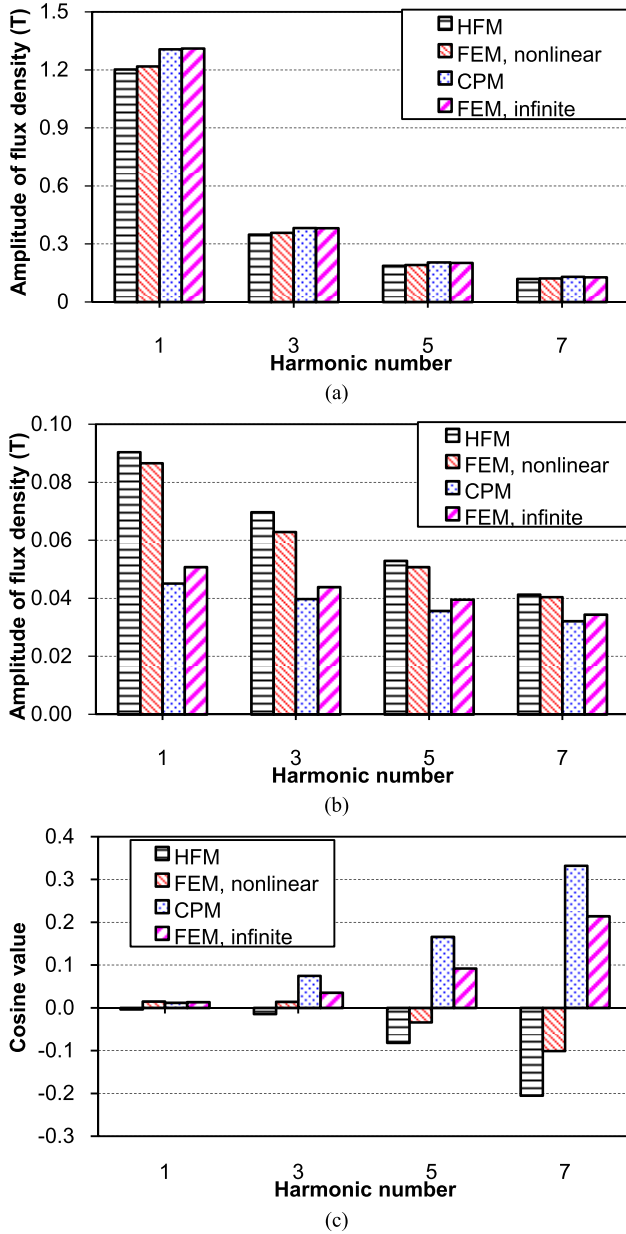


Fig. 21. Harmonic component of HFM, CPM, and FEM predicted cogging torques of Machine A at eight electrical degrees. (a) Amplitude of radial flux density. (b) Amplitude of circumferential flux density. (c) Cosine value of phase difference.

errors. It is caused by the deformations in the magnets and the circular path to predict the air-gap flux density when the slotted domain is mapped to the slotless domain in the conformal mapping [36]. The low accuracy of the model for cogging torque can also be explained in Fig. 21. For Machine A, the harmonic amplitude of flux density and the harmonic cosine value of phase difference of flux density are calculated using (45). It can be seen that the harmonic amplitude of flux density is accurate but the harmonic cosine values, i.e., $\cos[nm(\alpha_{an}-\alpha_{rn})]$, introduce large errors. Thus, the phase difference of flux density is mainly responsible for the cogging torque error.

Every model has its own advantage and application, and the proposed HFM is suitable for accurately calculating the

TABLE II
COMPARISON OF COMPUTATION TIME BETWEEN
CPM, HFM, AND FEM (UNIT: s)

Time	Machine A	Machine B	Machine C
CPM	1.6	1.6	11
HFM	18	20	27
FEM, nonlinear	170	175	306

air-gap flux density, flux linkage, and back EMF considering the saturation effect. There are other models to predict cogging torque more accurately, such as the exact conformal mapping method or the subdomain model [9]–[11], [36]. However, these models are very time consuming. Besides, the saturation effect is neglected in these models. Therefore, all these models and methods are complimentary and provide options for electric machine researchers and engineers aiming at different targets.

The computation times of HFM, CPM, and FEM for predicting back EMF and cogging torque using the same computer are shown in Table II. It should be noted that FEM is performed on a commercial FE platform of Ansys Maxwell, while two others are performed by using MATLAB script. In HFM and CPM, the number of points on the circular air-gap path is 720. The number of nodes in the MEC of HFM is 120. In FEM, the mesh distribution of Machines A, B, and C is shown in Fig. 7 and the number of nodes is 9012/9092/29436, respectively. The number of steps in one electrical period is set as 180/180/144, respectively. It is demonstrated that HFM is much faster than FEM for three machines. HFM can save nearly 7/8 computation time of FEM. This advantage of HFM is extremely significant for the initial design and optimization.

V. CONCLUSION

This paper has developed a nonlinear HFM to predict the magnetic field distribution and electromagnetic performance in SPM machines considering saturation. The HFM combines CPM with nonlinear MEC through the transformation from the magnetic potential distribution in the stator to the equivalent current on the stator bore. Iterative loop including CPM and MEC is carried out to predict the air-gap field distribution. From magnetic field prediction, the flux linkage and back EMF accounting for the flux leakage are computed. The excellent accuracy of HFM is validated by the FEM and experimental results. Besides, the comparison shows that HFM is much faster than FEM, which saves much time for machine design. As for the on-load condition, the analysis of magnetic field will be more complex, e.g., a) the saturation level will vary with the load and b) the superposition theory cannot be applied because of nonlinearity. However, since the proposed model is based on the combination of CPM and MEC, it can be extended to account for the armature-reaction field together with the saturation effect, which will be reported in a future paper.

ACKNOWLEDGMENT

This work was supported in part by the National Natural Science Foundation of China under Grant 51677169 and

Grant 51637009 and in part by the Fundamental Research Funds for the Central Universities under Grant 2017QNA4016.

REFERENCES

- [1] Z. Q. Zhu and D. Howe, "Electrical machines and drives for electric, hybrid, and fuel cell vehicles," *Proc. IEEE*, vol. 95, no. 4, pp. 746–765, Apr. 2007.
- [2] K. Komeza and M. Doms, "Finite-element and analytical calculations of no-load core losses in energy-saving induction motors," *IEEE Trans. Ind. Electron.*, vol. 59, no. 7, pp. 2934–2946, Jul. 2012.
- [3] Z. Q. Zhu, Y. Pang, D. Howe, S. Iwasaki, R. Deodhar, and A. Pride, "Analysis of electromagnetic performance of flux-switching permanent-magnet machines by nonlinear adaptive lumped parameter magnetic circuit model," *IEEE Trans. Magn.*, vol. 41, no. 11, pp. 4277–4287, Nov. 2005.
- [4] J. T. Chen, Z. Q. Zhu, and D. Howe, "A dual-lumped parameter magnetic circuit model accounting for the cross-coupling effect, with particular reference to flux-switching permanent magnet machines," in *Proc. 4th IET Conf. Power Electron., Mach. Drives*, Apr. 2008, pp. 111–115.
- [5] C. Mi, M. Filippa, W. Liu, and R. Q. Ma, "Analytical method for predicting the air-gap flux of interior-type permanent-magnet machines," *IEEE Trans. Magn.*, vol. 40, no. 1, pp. 50–58, Jan. 2004.
- [6] Z. Q. Zhu and D. Howe, "Instantaneous magnetic field distribution in brushless permanent magnet dc motors. Part II: Armature-reaction field," *IEEE Trans. Magn.*, vol. 29, no. 1, pp. 136–142, Jan. 1993.
- [7] D. Žarko, D. Ban, and T. A. Lipo, "Analytical calculation of magnetic field distribution in the slotted air gap of a surface permanent-magnet motor using complex relative air-gap permeance," *IEEE Trans. Magn.*, vol. 42, no. 7, pp. 1828–1837, Jul. 2006.
- [8] M. Hafner, D. Franck, and K. Hameyer, "Static electromagnetic field computation by conformal mapping in permanent magnet synchronous machines," *IEEE Trans. Magn.*, vol. 46, no. 8, pp. 3105–3108, Aug. 2010.
- [9] T. C. O'Connell and P. T. Krein, "A Schwarz–Christoffel-based analytical method for electric machine field analysis," *IEEE Trans. Energy Convers.*, vol. 24, no. 3, pp. 565–577, Sep. 2009.
- [10] K. Boughrara, R. Ibtouen, D. Žarko, O. Touhami, and A. Rezzoug, "Magnetic field analysis of external rotor permanent-magnet synchronous motors using conformal mapping," *IEEE Trans. Magn.*, vol. 46, no. 9, pp. 3684–3693, Sep. 2010.
- [11] K. Ramakrishnan, D. Žarko, A. Hanic, and G. Mastinu, "Improved method for field analysis of surface permanent magnet machines using Schwarz–Christoffel transformation," *IET Electr. Power Appl.*, vol. 11, no. 6, pp. 1067–1075, Jul. 2017.
- [12] S. G. Min, G. Bramerdorfer, and B. Sarlioglu, "Analytical modeling and optimization for electromagnetic performances of fractional-slot PM brushless machines," *IEEE Trans. Ind. Electron.*, vol. 65, no. 5, pp. 4017–4027, May 2018.
- [13] Z. J. Liu and J. T. Li, "Analytical solution of air-gap field in permanent-magnet motors taking into account the effect of pole transition over slots," *IEEE Trans. Magn.*, vol. 43, no. 10, pp. 3872–3883, Oct. 2007.
- [14] F. Dubas and C. Espanet, "Analytical solution of the magnetic field in permanent-magnet motors taking into account slotting effect: No-load vector potential and flux density calculation," *IEEE Trans. Magn.*, vol. 45, no. 5, pp. 2097–2109, May 2009.
- [15] T. Lubin, S. Mezani, and A. Rezzoug, "Exact analytical method for magnetic field computation in the air gap of cylindrical electrical machines considering slotting effects," *IEEE Trans. Magn.*, vol. 46, no. 4, pp. 1092–1099, Apr. 2010.
- [16] L. J. Wu, Z. Q. Zhu, D. Staton, M. Popescu, and D. Hawkins, "An improved subdomain model for predicting magnetic field of surface-mounted permanent magnet machines accounting for tooth-tips," *IEEE Trans. Magn.*, vol. 47, no. 6, pp. 1693–1704, Jun. 2011.
- [17] Y. Oner, Z. Q. Zhu, L. J. Wu, X. Ge, H. Zhan, and J. T. Chen, "Analytical on-load subdomain field model of permanent-magnet Vernier machines," *IEEE Trans. Magn.*, vol. 63, no. 7, pp. 4105–4117, Jul. 2016.
- [18] H. Hu, J. Zhao, X. Liu, Y. Guo, and J. Zhu, "No-load magnetic field and cogging force calculation in linear permanent-magnet synchronous machines with semiclosed slots," *IEEE Trans. Ind. Electron.*, vol. 64, no. 7, pp. 5564–5575, Jul. 2017.
- [19] A. Dalal, S. Nekkalapu, and P. Kumar, "2-D analytical subdomain model for hybrid dual-rotor motor," *IEEE Trans. Magn.*, vol. 52, no. 6, Jun. 2016, Art. no. 8103609.
- [20] A. Hemeida and P. Sergeant, "Analytical modeling of surface PMSM using a combined solution of Maxwell's equations and magnetic equivalent circuit," *IEEE Trans. Magn.*, vol. 50, no. 12, Dec. 2014, Art. no. 7027913.
- [21] M. Hafner, D. Franck, and K. Hameyer, "Accounting for saturation in conformal mapping modeling of a permanent magnet synchronous machine," *COMPEL-Int. J. Comput. Math. Elect. Electron. Eng.*, vol. 30, no. 3, pp. 916–928, 2011.
- [22] H. Mahmoud, N. Bianchi, G. Bacco, and N. Chiodetto, "Nonlinear analytical computation of the magnetic field in reluctance synchronous machines," *IEEE Trans. Ind. Appl.*, vol. 53, no. 6, pp. 5373–5382, Nov./Dec. 2017.
- [23] F. R. Alam and K. Abbaszadeh, "Magnetic field analysis in eccentric surface-mounted permanent-magnet motors using an improved conformal mapping method," *IEEE Trans. Energy Convers.*, vol. 31, no. 1, pp. 333–344, Mar. 2016.
- [24] K. Abbaszadeh and F. Rezaee-Alam, "On-load field component separation in surface-mounted permanent-magnet motors using an improved conformal mapping method," *IEEE Trans. Magn.*, vol. 52, no. 2, Feb. 2016, Art. no. 5200112.
- [25] F. Rezaee-Alam, B. Rezaealam, and J. Faiz, "Unbalanced magnetic force analysis in eccentric surface permanent-magnet motors using an improved conformal mapping method," *IEEE Trans. Energy Convers.*, vol. 32, no. 1, pp. 146–154, Mar. 2017.
- [26] A. Hanic, D. Zarko, and Z. Hanic, "A novel method for no-load magnetic field analysis of saturated surface permanent-magnet machines using conformal mapping and magnetic equivalent circuits," *IEEE Trans. Energy Convers.*, vol. 31, no. 2, pp. 740–749, Jun. 2016.
- [27] Y. Laoubi, M. Dhifli, G. Verez, Y. Amara, and G. Barakat, "Open circuit performance analysis of a permanent magnet linear machine using a new hybrid analytical model," *IEEE Trans. Magn.*, vol. 51, no. 3, Mar. 2015, Art. no. 8102304.
- [28] R. L. J. Sprangers, J. J. H. Paulides, B. L. J. Gysen, and E. A. Lomonova, "Magnetic saturation in semi-analytical harmonic modeling for electric machine analysis," *IEEE Trans. Magn.*, vol. 52, no. 2, Feb. 2016, Art. no. 8100410.
- [29] P. Liang, F. Chai, L. Chen, and Y. Wang, "Analytical prediction of no-load stator iron losses in spoke-type permanent-magnet synchronous machines," *IEEE Trans. Energy Convers.*, vol. 33, no. 1, pp. 252–259, Mar. 2018.
- [30] L. Roubache, K. Boughrara, F. Dubas, and R. Ibtouen, "New subdomain technique for electromagnetic performances calculation in radial-flux electrical machines considering finite soft-magnetic material permeability," *IEEE Trans. Magn.*, vol. 54, no. 4, Apr. 2018, Art. no. 8103315.
- [31] Z. Q. Zhu, D. Howe, and C. C. Chan, "Improved analytical model for predicting the magnetic field distribution in brushless permanent-magnet machines," *IEEE Trans. Magn.*, vol. 38, no. 1, pp. 229–238, Jan. 2002.
- [32] D. Žarko, D. Ban, and T. A. Lipo, "Analytical solution for cogging torque in surface permanent-magnet motors using conformal mapping," *IEEE Trans. Magn.*, vol. 44, no. 1, pp. 52–65, Jan. 2008.
- [33] X. Huang, M. Zhu, W. Chen, J. Zhang, and Y. Fang, "Dynamic reluctance mesh modeling and losses evaluation of permanent magnet traction motor," *IEEE Trans. Magn.*, vol. 53, no. 6, Jun. 2017, Art. no. 8102804.
- [34] G. Liu, S. Jiang, W. Zhao, and Q. Chen, "A new modeling approach for permanent magnet Vernier machine with modulation effect consideration," *IEEE Trans. Magn.*, vol. 53, no. 1, pp. 1–12, Jan. 2017.
- [35] A. Dalal and P. Kumar, "Analytical model for permanent magnet motor with slotting effect, armature reaction, and ferromagnetic material property," *IEEE Trans. Magn.*, vol. 51, no. 12, Dec. 2015, Art. no. 8114910.
- [36] L. J. Wu, Z. Q. Zhu, D. A. Staton, M. Popescu, and D. Hawkins, "Comparison of analytical models of cogging torque in surface-mounted PM machines," *IEEE Trans. Ind. Electron.*, vol. 59, no. 6, pp. 2414–2425, Jun. 2012.

L. J. Wu (M'11–SM'14) received the B.Eng. and M.Sc. degrees in electrical engineering from the Hefei University of Technology, Hefei, China, in 2001 and 2004, respectively, and the Ph.D. degree in electrical engineering from The University of Sheffield, Sheffield, U.K., in 2011.

From 2004 to 2007, he was an Engineer with Delta Electronics (Shanghai) Co., Ltd., Shanghai, China. From 2012 to 2013, he was a Design Engineer with the Sheffield Siemens Wind Power Research Center, Sheffield, where he was involved in wind power generators. From 2013 to 2016, he was an Advanced Engineer with Siemens Wind Power A/S, Brande, Denmark. Since 2016, he has been with Zhejiang University, Hangzhou, China, where he is currently a Professor of electrical machines and control systems. His current research interests include the design and control of permanent-magnet machines.

Zhaokai Li received the B.E. degree in electrical engineering from Zhejiang University, Hangzhou, China, in 2015, where he is currently pursuing the Ph.D. degree in motor design.

His current research interests include the design of permanent-magnet machines and analysis of iron loss in the electrical machines.

Xiaoyan Huang (M'09) received the B.E. degree in control measurement techniques and instrumentation from Zhejiang University, Hangzhou, China, in 2003, and the Ph.D. degree in electrical machines and drives from the University of Nottingham, Nottingham, U.K., in 2008.

From 2008 to 2009, she was a Research Fellow with the University of Nottingham. She is currently a Professor with the College of Electrical Engineering, Zhejiang University, where she is involved in electrical machines and drives. Her current research interests include permanent-magnet machines and drives for aerospace and traction applications, and generator system for urban networks.

Yunlong Zhong received the B.E. degree in electrical engineering from Zhejiang University, Hangzhou, China, in 2013, where he is currently pursuing the Ph.D. degree in electrical machines and drives.

His current research interests include design magnetic bearing.

Youtong Fang (M'11–SM'15) received the B.S. degree and Ph.D. degree in electrical engineering from the Hebei University of Technology, Hebei, China, in 1984 and 2001, respectively.

He is currently a Professor with the College of Electrical Engineering, Zhejiang University, Hangzhou, China. His current research interests include the application, control, and design of electrical machines.

Z. Q. Zhu (M'90–SM'00–F'09) received the B.Eng. and M.Sc. degrees in electrical and electronics engineering from Zhejiang University, Hangzhou, China, in 1982 and 1984, respectively, and the Ph.D. degree in electronic and electrical engineering from The University of Sheffield, Sheffield, U.K., in 1991.

Since 1988, he has been with The University of Sheffield, where he has been a Professor of electrical machines and control systems since 2000. He is currently the Head of the Electrical Machines and Drives Research Group, The University of Sheffield, where he is also a Royal Academy of Engineering/Siemens Research Chair. His current research interests include the design and control of permanent-magnet brushless machines and drives for applications ranging from automotive to renewable energy.